Strategies for the selective loading of patchy worm-like micelles with functional nanoparticles

Schöbel, Judith; Hils, Christian; Weckwerth, Anne; Schlenk, Mathias; Bojer, Carina; Stuart, Marc C. A.; Breu, Josef; Förster, Stephan; Greiner, Andreas; Karg, Matthias

Published in:
Nanoscale

DOI:
10.1039/c8nr05935g

Publication date:
2018

Nanoscale

PAPER

View Article Online
View Journal | View Issue

Cite this: *Nanoscale*, 2018, **10**, 18257

Strategies for the selective loading of patchy worm-like micelles with functional nanoparticles†

Judith Schöbel,[a] Christian Hils,[a] Anne Weckwerth,[b] Mathias Schlenk,[b] Carina Bojer,[c] Marc C. A. Stuart,[d] Josef Breu,[c,e] Stephan Förster,‡[b] Andreas Greiner,[a,e] Matthias Karg §[b] and Holger Schmalz *[a,e]

Block copolymer self-assembly in solution paves the way for the construction of well-defined compartmentalized nanostructures. These are excellent templates for the incorporation and stabilisation of nanoparticles (NPs), giving rise to highly relevant applications in the field of catalysis or sensing. However, the regio-selective incorporation of NPs in specific compartments is still an issue, especially concerning the loading with different NP types. Using crystallisation-driven self-assembly (CDSA), functional worm-like crystalline-core micelles (wCCMs) with a tailor-made, nanometre-sized patchy corona were prepared as versatile templates for the incorporation and stabilisation of metal and metal oxide NPs. Different strategies, like ligand exchange or co-precipitation of polymer stabilised NPs with one surface patch, were developed that allow the incorporation of NPs in specific regions of the patchy wCCM corona. Independent of the NP type and the incorporation method, the NPs showed no tendency for agglomeration and were fixed within the corona patches of the wCCMs. The binary loading of patchy micelles with metal and metal oxide NPs was realised by combining different loading strategies, yielding hybrids with homogeneously dispersed NPs guided by the patchy structure of the template.

Received 23rd July 2018,
Accepted 11th September 2018

DOI: 10.1039/c8nr05935g

rsc.li/nanoscale

Introduction

A major challenge of today's materials science is the developing miniaturisation, demanding precisely tuneable micro- and nanostructures. The self-assembly of amorphous block copolymers (BCPs) in solution proved to be an excellent tool to meet these demands, as a myriad of tailor-made micellar morphologies is accessible.[1] Spherical, cylindrical and helical micelles as well as vesicles are easily obtained by the use of selective solvents.[2–6] More complex preparation steps involving crosslinking or guided hierarchical self-assembly protocols enable the formation of Janus, patchy and multicompartment micelles (MCMs).[7–14] Among the MCMs, common examples include clover-, hamburger-, raspberry- and football-like micelles, as well as one-dimensional supracolloidal polymer chains.[15–18] Moreover, MCMs serve as building blocks for the formation of hierarchical superstructures, opening the way for applications in optoelectronic devices, in drug delivery or as templates for selective nanoparticle (NP) incorporation.[9,19–22] Although these state-of-the-art methods give access to manifold micelle morphologies, the preparation of well-defined cylindrical or worm-like micelles remains a challenge, as in general the length of the micelles cannot be precisely controlled, leading to broad length distributions.

To overcome these limitations in length control, crystallisation-driven self-assembly (CDSA) gained increasing attention since it is a powerful and very flexible method.[15,23] Similar to living polymerisation, CDSA can be conducted in a living manner, *i.e.*, the ends of the cylindrical micelles remain active for the addition of unimers (molecularly dissolved BCPs bearing a crystallisable block). This was first reported by Manners and Winnik *et al.* who self-assembled poly(ferrocenyl dimethylsilane) (PFS) containing BCPs.[24,25] Using a seeded-

[a]*Makromolekulare Chemie II, Universität Bayreuth, 95440 Bayreuth, Germany. E-mail: holger.schmalz@uni-bayreuth.de*
[b]*Physikalische Chemie I, Universität Bayreuth, 95440 Bayreuth, Germany*
[c]*Anorganische Chemie I, Universität Bayreuth, 95440 Bayreuth, Germany*
[d]*Stratingh Institute for Chemistry and Electron Microscopy, Group Groningen, Biomolecular Sciences and Biotechnology Institute, University of Groningen, 9747 AG Groningen, The Netherlands*
[e]*Bavarian Polymer Institute (BPI), Universität Bayreuth, 95440 Bayreuth, Germany*

†Electronic supplementary information (ESI) available: Additional characterisation data and TEM micrographs of hybrid micelles. See DOI: 10.1039/c8nr05935g

‡Present address: JCNS-1/ICS-1, Forschungszentrum Jülich, 52425 Jülich, Germany.
§Present address: Physikalische Chemie I, Heinrich-Heine-Universität Düsseldorf, 40204 Düsseldorf, Germany.

growth protocol, living CDSA enables a precise length control and opens the way for different micellar architectures like block comicelles (in analogy to BCPs), branched micelles, gradient block comicelles and hierarchical self-assemblies.[26–36] In addition to PFS containing BCPs, a variety of other semi-crystalline polymers were reported to undergo CDSA, *e.g.* polyethylene (PE),[37,38] poly(L-lactide),[39,40] poly(3-hexylthiophene)[41,42] and poly(ε-caprolactone).[43,44] Recently, we have shown that worm-like crystalline-core micelles (wCCMs) with a patch-like microphase-separated corona can be prepared by CDSA of polystyrene-*block*-polyethylene-*block*-poly(methyl methacrylate) (SEM) triblock terpolymers.[45,46] Here, the micellar corona is made of alternating nanometre-sized polystyrene (PS) and poly(methyl methacrylate) (PMMA) patches and the semi-crystalline PE block forms the core. The concept of living CDSA was successfully transferred to the self-assembly of SEM triblock terpolymers employing spherical crystalline-core micelles (sCCMs) as seeds, giving access to patchy micelles with controlled length and length distribution as well as more complex architectures like patchy block comicelles.[47]

Compartmentalised micelles are ideal templates for hybrid materials with inorganic NPs, as the structural complexity allows for a regio-selective incorporation of the NPs.[20,48] This opens the way for applications in the biomedical sector (drug delivery, imaging), in the optoelectronic sector (nanodevices, photovoltaics) or in sensing and catalysis.[49–58] Different hybrid materials derived from amorphous MCMs as well as crystalline-core micelles have been reported.[52,53,55,57,59–65] However, these publications are mainly focused on the incorporation of only one type of NP, as the binary loading of compartmentalised micelles still remains a challenge and is hardly reported.[66,67] The unique patchy structure of the SEM wCCM corona provides an excellent platform for the construction of tailor-made binary loaded hybrid materials, but this demands the efficient functionalisation of at least one of the corona forming blocks. Recently, we have reported the post-polymerisation amidation of the PMMA block of SEM triblock terpolymers using a 30-fold excess of different *N*,*N*-dialkylethylenediamines (alkyl = methyl, ethyl, iso-propyl).[68] This method showed some disadvantages regarding the harsh reaction conditions (≥60 h at 130 °C), the formed side products and the required large excess of amine. In particular, the formation of a large fraction of imide units (*ca.* 50 mol% with respect to the consumed PMMA units) resulted in low functionalisation degrees and limited solubility in organic solvents, especially for more polar *N*,*N*-dialkylethylenediamines (alkyl = methyl, ethyl). The limited solubility affected the CDSA and led to ill-defined, short wCCMs for degrees of functionalisation above 20% for the dimethyl derivative. Thus, only for nonpolar, sterically hindered alkyl substituents (iso-propyl groups) well-defined patchy wCCMs with a reasonable degree of functionalisation (f = 55%) could be obtained. As a result, the first loading experiments with NPs revealed only a partial and inhomogeneous loading, most probably due to the insufficient functionalisation of the amidated patches.

Here, we report the use of functionalised patchy wCCMs as versatile templates for the regio-selective incorporation of NPs. This is realised by amidation of the PMMA block of SEM triblock terpolymers with activated *N*,*N*-dimethylethylenediamine (DMEDA), resulting in a nearly quantitative amidation. CDSA of the amidated SEM triblock terpolymers produces the desired patchy wCCMs, featuring highly functionalised corona patches for NP stabilisation. Different strategies for the regio-selective loading of the amidated as well as non-functional PS patches with metal and metal oxide NPs are employed to yield the defined hybrid micelles. Finally, we present the successful binary loading of the patchy wCCMs with two different types of NPs (gold/zinc oxide and gold/silver).

Experimental

Materials

All chemicals were purchased from Sigma-Aldrich unless otherwise noted. Tetrahydrofuran (THF) was dried over calcium hydride and potassium prior to use and DMEDA (Acros Organics) over calcium hydride. Ethanol (99.5%), *n*-heptane, acetic acid (99.9%), L-Selectride (1 M in THF), *n*-butyllithium (*n*-BuLi, 2.5 M in hexane), PMMA (M_w = 35 kg mol^{-1}, Acros Organics), tetrachloroauric acid trihydrate ($HAuCl_4 \cdot 3H_2O$, Alfa Aesar), silver trifluoroacetate (AgTFA), zinc acetate dihydrate, copper acetate, sodium hydroxide and lithium hydroxide monohydrate were used as received.

SEM triblock terpolymers

The SEM triblock terpolymers were synthesised by a combination of living anionic polymerisation and catalytic hydrogenation, as published elsewhere.[68] The composition of the employed SEM triblock terpolymers is $S_{40}E_{21}M_{39}{}^{108}$ and $S_{48}E_{27}M_{25}{}^{141}$. In this notation, the subscripts describe the mass fraction of the corresponding block in wt% and the superscript denotes the overall molecular weight in kg mol^{-1}.

Amidation of SEM

The PMMA block of the SEM triblock terpolymers was amidated under an inert argon atmosphere. First, DMEDA (2 equivalents with respect to MMA units of SEM) was dissolved in 20 mL dry THF and cooled to −78 °C by using an acetone/dry ice bath. To this solution, *n*-BuLi (equimolar amount with respect to DMEDA) was added dropwise under stirring followed by heating to room temperature. In another flask, 1 g SEM (3.9 mmol MMA units for $S_{40}E_{21}M_{39}{}^{108}$ and 2.5 mmol for $S_{48}E_{27}M_{25}{}^{141}$, 1 equivalent) was dissolved in 80 mL anhydrous THF at 65 °C for 30 min. Subsequently, the solution was cooled to 40 °C and the activated amine solution was added. The reaction was allowed to proceed for 24 h at 40 °C under stirring. Then, 1 mL of deionised water was added to deactivate excess amine and the obtained amidated SEM triblock terpolymers (SEDMA) were isolated by precipitation from pentane. For purification, the product was dissolved in THF at 65 °C (c = 10 g L^{-1}) and centrifuged at 40 °C and 5000 rpm for

15 min in order to remove residual lithium hydroxide. The supernatant was precipitated from pentane and dried in a vacuum oven (yield: 1 g (83%)).

Formation of patchy wCCMs

The functional, patchy wCCMs were prepared by CDSA of the amidated SEDMA triblock terpolymers in THF. To this end, the triblock terpolymers were dissolved in THF (c = 10 g L^{-1}) at 65 °C for 30 min and subsequently cooled to T_c = 20 °C (*s*-SEDMA) or T_c = 25 °C (*as*-SEDMA) in a thermostated shaker unit (HLC-MKR 13, Ditabis). The self-assembly process was allowed to proceed for 24 h at a shaking rate of 200 rpm.

Synthesis of zinc oxide (ZnO) and copper oxide (CuO) NPs

The synthesis of ZnO and CuO NPs was conducted according to previously published protocols.[69,70] For the preparation of ZnO NPs, 0.04 mol zinc acetate (1 equivalent) was added to 400 mL boiling ethanol in order to dissolve the salt. After cooling the solution to room temperature, a lithium hydroxide monohydrate solution in ethanol (400 mL, c = 140 mM, 1.4 equivalents) was added and the reaction mixture was immediately cooled to 0 °C. The ZnO NPs were precipitated from *n*-heptane and redispersed in ethanol to yield a final concentration of c = 3.8 g L^{-1}. The average diameter obtained from transmission electron microscopy (TEM) was D = 2.7 ± 0.4 nm.

The CuO NPs were synthesised by dissolving 5 mmol copper acetate (1 equivalent), 20 mmol sodium hydroxide (4 equivalents) and 10 mmol acetic acid (2 equivalents) in 500 mL ethanol. The reaction mixture was heated to 78 °C for 1 h to yield the CuO NPs. The CuO NP dispersion was precipitated from *n*-heptane and redispersed in ethanol to yield a final concentration of c = 1 g L^{-1}. The average diameter of the CuO NPs was determined to be D = 3.8 ± 0.6 nm by TEM. The full characterisation of the NPs can be found in the ESI (Fig. S1†).

Loading of patchy wCCMs *via* ligand exchange

To 2 mL of a wCCM dispersion (c = 1 g L^{-1}, THF) 75 μL of the ZnO NP dispersion (c = 3.8 g L^{-1}, ethanol) were added and the solution was stirred for 24 h. The same procedure was used for the incorporation of CuO NPs, employing 150 μL of the CuO NP dispersion (c = 1 g L^{-1}, ethanol).

In situ synthesis of gold (Au) and silver (Ag) NPs in patchy wCCMs

To 2 mL of a wCCM dispersion (c = 1 g L^{-1}, THF) 40 μL of the corresponding acid ($HAuCl_4 \cdot 3H_2O$) or metal salt (AgTFA) dissolved in THF (c = 0.1 M) were added. Immediately, 20 μL of L-Selectride (c = 1 M, THF) were added and the successful formation of the respective metal NPs was indicated by a characteristic colour change. For *as*-SEDMA the employed amounts of AgTFA and L-Selectride were reduced by half.

Continuous *in situ* loading of SEDMA wCCMs with Au NPs

The continuous, *in situ* loading of *s*-SEDMA wCCMs was accomplished by a PTFE based microfluidic chip with one main channel and four separate side channels for controlled fluid double focusing. The microfluidic channels of the inner mixing part had a diameter of D = 500 μm. The outer chip holes were bigger with a diameter of D = 1000 μm in order to connect the five inlets *via* polyethylene (PE) tubes to the syringe pumps. The outlet was fixed to a glass capillary, which was used to run and investigate the laminar flow controlled synthesis at a distance of 5 cm *via* optical microscopy. In a typical experiment, the main channel was fed with an *s*-SEDMA wCCM dispersion (c = 1 g L^{-1}, THF) at a flow rate of 2000 μL h^{-1}. The first two side channels were run with a $HAuCl_4 \cdot 3H_2O$ solution (c = 2 mM, THF) at a flow rate of 2000 μL h^{-1} and the second two side channels with an L-Selectride solution (c = 20 mM, THF) at a flow rate of 1000 μL h^{-1}.

Synthesis of PS-stabilised Au NPs (PS@Au)

PS@Au NPs were prepared *via* ligand exchange starting from citrate-stabilised Au NPs (D = 7.9 ± 0.7 nm), synthesised *via* a seeded growth method reported by Piella *et al.*[71] A detailed characterisation of the citrate-stabilised Au NPs can be found in the ESI (Fig. S2†). A trithiocarbonate terminated PS (PS-TTC, M_n = 10 400 g mol^{-1}, $Đ$ = 1.05, determined by gel permeation chromatography (GPC), ESI Fig. S3A†) was synthesised *via* reversible addition–fragmentation chain transfer (RAFT) polymerisation according to a previously published protocol.[72] UV-Vis spectroscopy confirmed the presence of the characteristic TTC absorption at λ = 315 nm (ESI Fig. S3B†). 120 mL of the aqueous dispersion of citrate-stabilised Au NPs were overlaid with 40 mL of the PS-TTC solution in toluene (c = 10 mM). After 2 h of vigorous stirring, the phase-transfer of the Au NPs was completed, *i.e.*, the aqueous phase was clear and colourless, whereas the toluene phase showed a deep red colour, indicating a successful ligand exchange. The toluene phase was separated and centrifuged at 12 000–14 000 rpm for 12 h to isolate the PS@Au NPs. The PS@Au NPs were purified from the remaining free PS-TTC ligand by eight washing and centrifugation cycles with 2 mL toluene, respectively. The absence of the free PS-TTC ligand was confirmed by GPC (ESI Fig. S4A†). The hydrodynamic radius of the PS@Au NPs was determined with dynamic light scattering to R_h = 14.9 ± 0.7 nm (ESI Fig. S4B†). The concentration after final dispersion in toluene was determined by UV-Vis spectroscopy to $c = 5.3 \times 10^{17}$ NP L^{-1} (see the ESI† for further details).

Loading of SEDMA wCCMs with PS@Au NPs by co-precipitation

10 μL of *s*-SEDMA wCCMs (c = 10 g L^{-1}, THF), 37 μL PS@Au NPs ($c = 5.3 \times 10^{17}$ NP L^{-1}, toluene) and 53 μL THF were mixed in a vial. To this solution, 40 μL of acetone were added in 4 steps under stirring with an equilibration time of 30 min, respectively. Subsequently, 860 μL of acetone were added to achieve an overall acetone fraction of 90 vol%. The solution was stirred for at least 2 h before analysis. In a second experiment, 50 μL of PS@Au NPs and 40 μL THF were employed. All other reaction conditions were kept constant.

Binary loading of SEDMA wCCMs

In a vial, 70 μL THF, 10 μL *s*-SEDMA wCCMs (c = 10 g L^{-1}, THF) and 7.5 μL ZnO NPs (c = 3.8 g L^{-1}, ethanol) were mixed and stirred for 1 h, followed by the addition of 27 μL PS@Au NPs ($c = 5.3 \times 10^{17}$ NP L^{-1}, toluene). To this solution, 40 μL of acetone were added in 4 steps with an equilibration time of 30 min, respectively. Subsequently, 845 μL of acetone were added to obtain an overall acetone fraction of 90 vol% and the solution was stirred for 2 h before analysis.

For the binary loading with Ag and PS@Au NPs, 100 μL of preformed *s*-SEDMA/Ag hybrid micelles in THF (c = 1 g L^{-1}), prepared by *in situ* reduction of AgTFA, were used. The loading with PS@Au NPs was done according to the procedure described for ZnO/PS@Au NP hybrid micelles.

Instruments

For the microfluidic experiments, syringe pumps (Nemysis Systems, Cetoni GmbH) were used and connected *via* PE tubes (Scientific Commodities, Inc.) to a home-made PTFE chip. A glass capillary (Hilgenberg GmbH) with an inner diameter of D = 980 μm was connected to the end of the PTFE chip to elongate the reaction pathway. The Au NP formation was followed with an optical microscope IX71 (Olympus Co.) equipped with a D7000 digital camera (Nikon GmbH).

^{1}H-NMR spectroscopy was conducted on a Bruker Ultrashield 300 system using deuterated chloroform as the solvent at 300 MHz.

FT-IR spectroscopy was performed on a Digilab Excalibur Series FTS system with a Miracle ATR unit of Pike Technologies. The spectra were recorded with a resolution of 4 cm^{-1} and 16 scans were averaged per sample.

For GPC in THF, SDV gel columns (300 × 8 mm, 5 μm particle size, PSS Mainz) with pore sizes of 10^5, 10^4, 10^3 and 10^2 Å were used, together with a refractive index detector (RI 101, Techlab Shodex) and a UV detector operating at λ = 254 nm (Knauer). The applied flow rate was 1 mL min^{-1} at 40 °C. Narrowly distributed PS standards and toluene as the internal reference were used for calibration.

GPC in hexafluoroisopropanol with potassium trifluoroacetate (8 g L^{-1}) was conducted on PFG gel columns (300 × 8 mm, 7 μm particle size, PSS Mainz) with 100 and 300 Å pore sizes using a flow rate of 0.5 mL min^{-1} at 23 °C. The signals were detected by using a Gynkotec SE-61 refractive index detector. For calibration, narrowly distributed PMMA standards and toluene as the internal reference were used.

For GPC in *N*,*N*-dimethylformamide with lithium bromide (5 g L^{-1}), GRAM columns (300 × 8 mm, 10 μm particle size, PSS Mainz) with 100 and 3000 Å pore sizes were used. The sample was analysed at a flow rate of 0.5 mL min^{-1} at 23 °C using a DAD VL + G1315C diode array UV detector (Agilent Technologies) operated at λ = 270 nm and 525 nm. Narrowly distributed PS standards and toluene as the internal reference were employed for calibration.

The thermal properties of the SEDMA wCCM dispersions were analysed by using a SETARAM micro-DSC III system. The samples (c = 10 g L^{-1} in THF) were measured in closed batch cells at a scanning rate of 0.5 K min^{-1} and THF was used as the reference.

For UV-Vis measurements a JASCO V630 spectrophotometer and fused quartz cuvettes (Hellma, d = 0.2 cm) were used. The samples were analysed in THF (c = 0.1 g L^{-1}) and acetone at room temperature, using the corresponding pure solvent for background subtraction, respectively. For the binary loaded sample pure acetone was used as the reference.

Elastic bright-field TEM was conducted on a Zeiss 922 Omega EFTEM (Zeiss NTS GmbH, Oberkochen, Germany) electron microscope operating at an acceleration voltage of 200 kV. A bottom mounted CCD camera system (Ultrascan 1000, Gatan) recorded the zero-loss filtered images, which were processed by the imaging software Gatan Digital Micrograph 3.9 for GMS 1.4. For high-angle annular dark field scanning transmission electron microscopy (HAADF-STEM), a Tecnai T20 system (FEI, Eindhoven, The Netherlands) was used operating at 200 keV. Energy dispersive X-ray (EDX) spectra were recorded with an Xmax 80 (Oxford Instruments) detector. The samples were diluted to 0.1 g L^{-1} and drop-coated onto carbon-coated copper grids. The solvent was blotted with filter paper and the samples were dried in a vacuum oven at 0.2 mbar and room temperature before staining with ruthenium tetroxide (RuO_4). The software ImageJ was used to determine particle sizes, wCCM lengths and patch sizes. At least 100 measurements were done to obtain representative average values.

Results and discussion

Functional wCCMs with amino group containing patches

The formation of hybrid materials of patchy wCCMs and NPs demands an efficient functionalisation of one of the corona blocks of the employed SEM triblock terpolymers. To this end, we chose an amidation of the PMMA block with *N*,*N*-dimethylethylenediamine (DMEDA), utilizing a prior activation of the amine with *n*-butyllithium (Scheme 1A).[73] Due to the activation, the amount of DMEDA could be decreased to a 2-fold excess with respect to the amount of methyl ester units in the PMMA block (in comparison with the 30-fold excess used in our previous report[68]) and nearly quantitative conversion was obtained after 24 h under mild conditions (40 °C). The functionalisation proceeds without degradation of the polymer backbone, as shown by gel permeation chromatography (GPC) of an amidated PMMA homopolymer, which was functionalised under identical conditions as the SEM triblock terpolymers (ESI Fig. S5†).

The amidated SEM triblock terpolymers were characterised by ^{1}H-NMR and FT-IR spectroscopy, as discussed exemplarily for the amidation of $S_{40}E_{21}M_{39}^{108}$ (the subscripts describe the mass fraction of the corresponding block in wt% and the superscript denotes the overall molecular weight in kg mol^{-1}). The signals in the ^{1}H-NMR spectrum can be clearly assigned to the typical proton signals of the amide (Fig. 1A). There is only a weak signal of not consumed PMMA ester units at

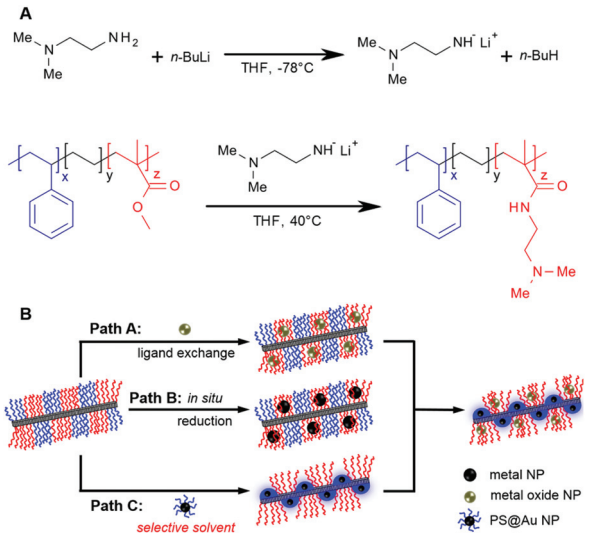

Scheme 1 Amidation of the SEM triblock terpolymers with prior activation of the amine by *n*-BuLi (A). Strategies for the regio-selective and binary loading of patchy wCCMs with metal and metal oxide NPs (B).

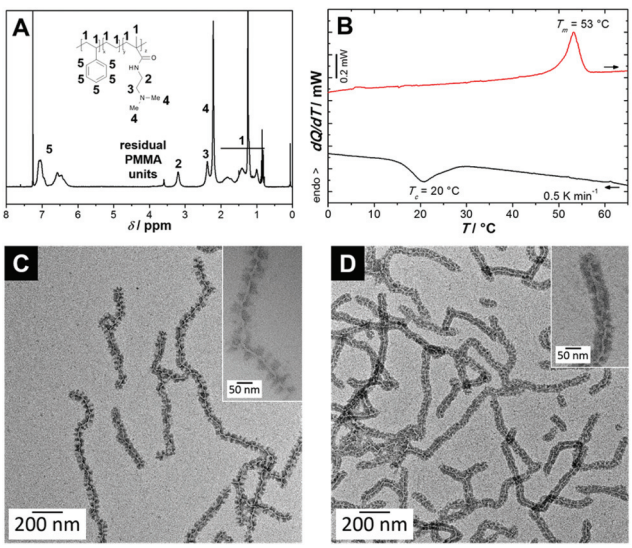

Fig. 1 ^{1}H-NMR spectrum recorded in $CDCl_3$ (A) and μDSC heating and cooling traces (c = 10 g L^{-1} in THF, (B)) of *s*-SEDMA as well as TEM micrographs of *s*-SEDMA (C) and *as*-SEDMA (D) wCCMs, selectively stained with RuO_4.

3.6 ppm. From the integral of this signal, calibrated by the aromatic polystyrene protons (5, 5 H), a degree of amidation of 95% results. Consequently, the composition and overall molecular weight of the functionalised triblock terpolymer changes to $S_{33}E_{17}DMA_{50}^{131}$. A signal for imide formation, which would be expected at 3.7–4 ppm,[68] is hardly observable. This indicates that the amidation proceeds without significant side reactions.

The successful amidation is further confirmed by FT-IR spectroscopy (ESI Fig. S6†), showing the characteristic amide I and amide II vibrations at 1660 cm^{-1} and 1526 cm^{-1}, respectively, and only a very weak C=O vibration of the remaining PMMA units. The negligible fraction of imide units in $S_{33}E_{17}DMA_{50}^{131}$ is supported by its solubility in tetrahydrofuran (THF) and chloroform ($CHCl_3$), as in the case of a large fraction of imide units the triblock terpolymer would be insoluble in both solvents.[68]

The solubility of the SEDMA triblock terpolymers in THF, which is used for CDSA, is crucial for the formation of well-defined patchy wCCMs. Recently, we have shown that the crystallisation temperature (T_c) of the PE middle block in solution is a very sensitive parameter to probe the solubility of the amidated triblock terpolymers.[68] With decreasing solubility an increase in the T_c of the PE block is observed with respect to that of the corresponding $S_{40}E_{21}M_{39}^{108}$ precursor (T_c = 21 °C). For T_c values above 30 °C only ill-defined and strongly aggregated wCCMs are formed. This is attributed to aggregation caused by the limited solubility of the amidated PMMA block, which results in a higher PE segment density and, thus, a better nucleation of PE crystallisation. Micro-differential scanning calorimetry (μDSC) shows a T_c at 20 °C for the synthesised $S_{33}E_{17}DMA_{50}^{131}$ triblock terpolymer (c = 10 g L^{-1} in THF, Fig. 1B), *i.e.*, almost identical to the SEM precursor underlining its good solubility in THF. Consequently, CDSA of $S_{33}E_{17}DMA_{50}^{131}$ in THF at 20 °C resulted in the formation of well-defined wCCMs with an average length of L = 540 ± 310 nm (Fig. 1C), as revealed by transmission electron microscopy (TEM). The sample was stained with RuO_4, which is known for selective staining of the PS domains. Therefore, the PS patches in the corona appear dark and the amidated PMMA (PDMA) patches appear bright, both being arranged in an almost alternating manner. The corona patches exhibit a similar width of 18 ± 5 nm for PS and 17 ± 5 nm for PDMA, respectively. Because of the symmetric structure (equally sized patches) of the corona, the amidated triblock terpolymer will be referred to as *s*-SEDMA in the following.

The patch sizes in the corona can be controlled by the composition of the triblock terpolymer. Hence, we probed the effect of patch size on NP incorporation by employing $S_{48}E_{27}M_{25}^{141}$, which shows an asymmetric block ratio of PS and PMMA with PMMA being the minority component. $S_{48}E_{27}M_{25}^{141}$ was amidated in analogy to $S_{40}E_{21}M_{39}^{108}$ and quantitative functionalisation is confirmed by ^{1}H-NMR (ESI Fig. S7A†). The composition of the triblock terpolymer changes to $S_{43}E_{23}DMA_{34}^{161}$ (*as*-SEDMA). Crystallisation at T_c = 25 °C resulted in well-defined patchy wCCMs with an average length of 660 ± 370 nm (Fig. 1D, ESI Fig. S7B†). Due to the lower PDMA content in the corona the patch widths change to 20 ± 6 nm for the PS patches and 14 ± 4 nm for the PDMA patches, respectively.

Selective loading of patchy wCCMs with NPs

The unique alternating structure of the functional patchy corona of SEDMA wCCMs offers the possibility to incorporate two different types of NPs. The patchy morphology guarantees an efficient separation and at the same time a dense packing

of single NPs. We developed three different strategies for the selective loading of the patches with metal and metal oxide NPs (Scheme 1B). Path A is based on selective interactions between the PDMA corona patch and the metal oxide NP, which are known to undergo ligand exchange if amino groups are offered.[74] Path B deals with the *in situ* synthesis of metal NPs within the PDMA patch of the SEDMA wCCMs, which provides tertiary amino groups as anchor groups for the efficient stabilisation of different metal NPs like gold (Au) or silver (Ag).[75] Path C is based on polymer–polymer and polymer–solvent interactions. The addition of a selective solvent for one of the corona patches leads to the collapse of the other corona patch. Thus, NPs that are stabilised with the same polymer as the collapsing corona patch are incorporated into the collapsing patch upon selective solvent addition. Combination of path A and C finally leads to binary loaded wCCMs.

Following path A, we investigated the ligand exchange for zinc oxide (ZnO) and copper oxide (CuO) NPs. Both types of NPs were synthesised in ethanol with acetate ligands for stabilisation and have average diameters of D = 2.7 ± 0.4 nm for ZnO and D = 3.8 ± 0.6 nm for CuO (determined by TEM, ESI Fig. S1†). The obtained NPs are phase pure according to the powder X-ray diffraction patterns (ESI Fig. S1A†) and exhibit a narrow particle size distribution (ESI Fig. S1B†). The concentration of the NP dispersions was adjusted to 1–4 g L^{-1}, which ensures that the total amount of added NP dispersion is less than 10 vol% with respect to the employed THF dispersion of SEDMA wCCMs. For higher volume fractions of ethanol the wCCMs are insoluble and agglomerate before the ligand exchange is completed. The NP incorporation was finished after 1 d and the *s*-SEDMA wCCMs were highly loaded with both types of NPs as revealed by TEM (ZnO: Fig. 2A and C; CuO: Fig. 2E), pointing to a successful ligand exchange, *i.e.*, acetate ligands *vs.* amino groups in the PDMA patch. The absence of free NPs in the TEM micrographs points to a complete incorporation of the ZnO and CuO NPs in the micellar corona.

The theoretical ZnO and CuO contents in the hybrid micelles, assuming a complete incorporation of the NPs in the micellar corona, are 12 wt% and 7 wt%, respectively. Both the ZnO and CuO NPs are homogeneously distributed within the PDMA patches of the *s*-SEDMA wCCMs without agglomeration and the "empty" PS patches are still clearly discernible. Here, it has to be noted that in contrast to the neat *s*-SEDMA wCCMs the hybrid micelles were analysed without prior staining with RuO_4, as the incorporated NPs provide an intrinsic staining of the patches. The UV-Vis spectra of the neat wCCMs show a continuous increase in absorbance with decreasing wavelength, which is attributed to scattering from the wCCMs (Fig. 2B and F). This is supported by the blue colour of the neat wCCM dispersion (Tyndall effect). The low wavelength part of the spectrum is dominated by a relatively weak absorption maximum at λ_{max} = 250 nm, deriving from the absorption of the PS units of the wCCMs. The UV-Vis spectra of the pure ZnO (Fig. 2B) and CuO (Fig. 2F) NPs show absorption maxima at approximately 300 nm, which overlap with the scattering contribution of the wCCMs. Consequently, the UV-Vis spectrum of the CuO NP hybrid micelles is similar to the spectrum of the neat *s*-SEDMA wCCMs (Fig. 2F). In contrast, the ZnO NPs show a pronounced shoulder at λ = 333 nm, which is also observable in the UV-Vis spectra of the ZnO NP loaded wCCMs (Fig. 2B), confirming the successful incorporation of the NPs in the patchy corona.

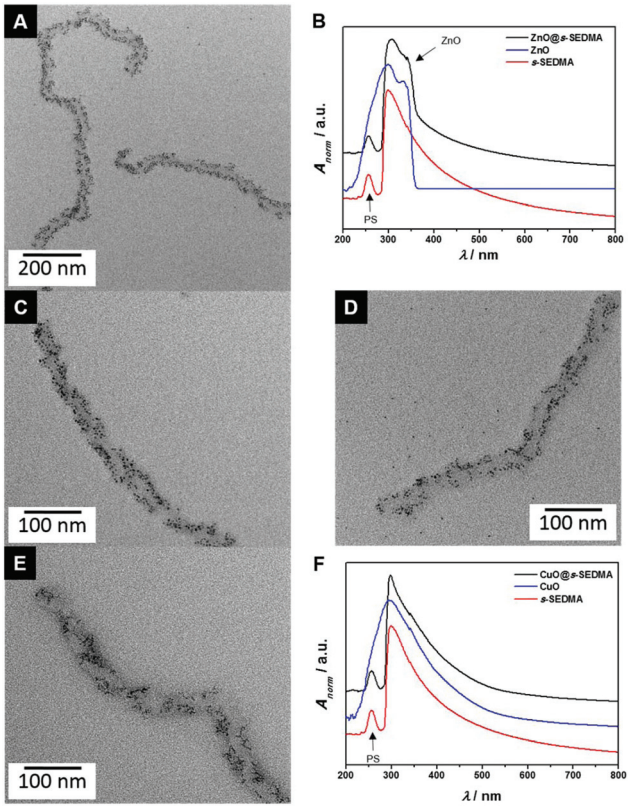

Fig. 2 TEM micrographs and the corresponding UV-Vis spectra for the hybrid micelles of *s*-SEDMA (A, B, C) and *as*-SEDMA (D) with ZnO, and *s*-SEDMA with CuO NPs (E, F). The UV-Vis spectra were shifted vertically for clarity.

To study the effect of patch size on the NP incorporation, we transferred the ligand exchange with ZnO NPs to the *as*-SEDMA wCCMs, keeping the amount of ZnO NPs constant. TEM clearly shows a decreased loading capacity for the smaller PDMA patches, supported by the observation of free ZnO NPs around the wCCMs (Fig. 2D, corresponding UV-Vis spectra in ESI Fig. S8A†). To further strengthen the effect of patch size, we added acetone as a selective solvent for the PDMA patch. This leads to a collapse of the PS patches and a swelling of the PDMA patches (ESI Fig. S9†). Due to the swelling, more ZnO NPs were incorporated into the corona and the PS patches are hardly observable.

In path B we utilised the functionalised corona patches as nanoreactors for the simultaneous stabilisation and *in situ* syntheses of different metal NPs *via* reduction of the corresponding acids and metal salts, *i.e.*, tetrachloroauric acid trihydrate ($HAuCl_4 \cdot 3H_2O$) and silver trifluoroacetate (AgTFA), with L-Selectride (lithium tri-*sec*-butylborohydride). We chose

L-Selectride since it is a mild reduction agent that does not reduce ester or amide groups.[76] After the addition of L-Selectride, the typical colour change of all solutions indicated a successful NP formation, which is further proven by the TEM micrographs shown in Fig. 3. The Au and Ag NPs show a spherical shape and are selectively incorporated into the patchy corona of the *s*-SEDMA (Fig. 3A and B) and *as*-SEDMA wCCMs (Fig. 3E and F). The diameters of the formed NPs are D_{Au} = 4.7 ± 1.2 nm and D_{Ag} = 2.9 ± 0.8 nm for the *s*-SEDMA and D_{Au} = 4.0 ± 1.3 nm and D_{Ag} = 2.2 ± 0.6 nm for the *as*-SEDMA hybrid micelles, respectively, as determined by TEM image analysis. The rather high size dispersity of the NPs might be attributed to the *in situ* reduction process, which does not allow a precise size control as nucleation and growth of the NPs happen almost simultaneously.

The PDMA patches in the SEDMA/Au hybrid micelles are highly loaded with Au NPs without showing any significant agglomeration. This can be ascribed to the nearly quantitative amidation of the PMMA block, resulting in a high density of amino anchor groups in the PDMA patches. We exemplarily analysed the loading capacity of the *s*-SEDMA wCCMs with Au NPs by inductively-coupled plasma optical emission spectroscopy (ICP-OES) and thermogravimetric analysis (TGA), which resulted in 652 μg and 787 μg Au, respectively. This equals to 25–28 wt% Au in the final hybrid micelles. Taking into account that the accuracy of ICP-OES fluctuates between 10–20%, the incorporation of Au by *in situ* synthesis can be regarded as nearly quantitative.[77] The high loading again provides an intrinsic staining of the PDMA patches, as already observed for the hybrid micelles prepared by ligand exchange. However, due to the similar width of both patch types the PS patches appear comparably small for the *s*-SEDMA based hybrid micelles, which makes it more difficult to discern the patchy structure of the corona. Nevertheless, for the *as*-SEDMA hybrid micelles the patches are clearly distinguishable, which can be attributed to the significantly smaller size of the PDMA patches (14 ± 4 nm) with respect to that of the PS patches (20 ± 6 nm) in the *as*-SEDMA wCCM corona. This underlines the excellent selectivity of the NP incorporation.

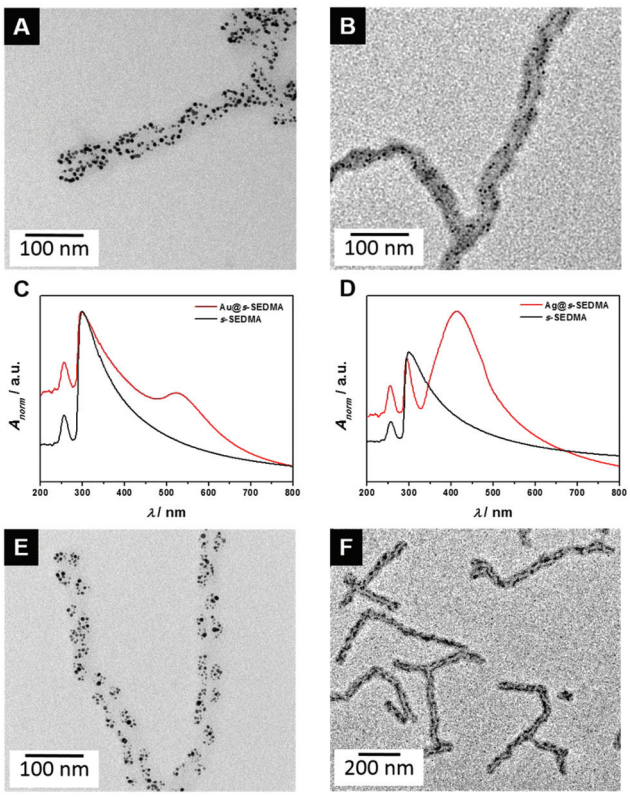

Fig. 3 Hybrid micelles obtained by *in situ* reduction. TEM micrographs and UV-Vis spectra of *s*-SEDMA/Au (A, C), *s*-SEDMA/Ag (B, D), and TEM micrographs of *as*-SEDMA/Au (E) and *as*-SEDMA/Ag (F).

Fig. 3C and S8B (ESI†) compare the UV-Vis spectra of the SEDMA wCCMs prior to and after the *in situ* synthesis of Au NPs. All absorbance spectra show the same spectral characteristics except for a peak at approximately λ_{max} = 523 nm that appears only for the Au NP loaded wCCMs. This peak can be assigned to absorption due to the localised surface plasmon resonance (LSPR) of the Au NPs, which is characteristic for small, spherical Au NPs.[78] The low absorbance at wavelengths of $\lambda \geq 700$ nm manifests the good stabilisation and distribution of the Au NPs by the wCCMs and the absence of Au NP aggregates.

Similar to the Au NPs, the Ag NPs are well distributed within the *s*-SEDMA and the *as*-SEDMA wCCMs without agglomeration (Fig. 3B and F). ICP-OES reveals a loading capacity of 103 μg Ag in the *s*-SEDMA wCCMs, which equals to 5 wt% in the final hybrid micelles (applied amount of Ag: 431 μg). The corona of both Ag hybrid micelles, *i.e.*, based on *s*- and *as*-SEDMA, again shows a patchy structure due to intrinsic staining of the PDMA patches by the incorporated Ag NPs. To highlight the selectivity of NP incorporation in the SEDMA wCCMs, we employed the *in situ* reduction method on the pure $S_{48}E_{27}M_{25}$[141] wCCMs (ESI Fig. S10†). The lack of functional groups in these wCCMs causes a statistical distribution of the Ag NPs over the whole TEM grid and almost no Ag NPs are located within the patchy corona. Furthermore, agglomeration of the Ag NPs is observed, which proves that functional groups for NP stabilisation are inevitable.

The UV-Vis spectra of the Ag NP loaded *s*-SEDMA (Fig. 3D) and *as*-SEDMA (ESI Fig. S8C†) wCCMs show a strong peak in absorbance at λ_{max} = 415–426 nm, superimposed to the wCCM absorbance. This peak is related to the LSPR of small, spherical Ag NPs.[79] Compared to the spectra of the Au NP loaded wCCMs, the Ag NP containing systems show a much stronger LSPR contribution, which is attributed to the higher absorption cross-section of Ag as compared to Au NPs of similar size. The narrow width of the LSPR resonance and the absence of significant absorbance at higher wavelengths again underline the good stabilisation and distribution of the Ag NPs by the wCCMs.

In order to study whether mixing effects have an influence on the *in situ* synthesis of NPs, we transferred the batch reduction to a continuous loading process, employing a micro-

fluidic chip with a double-focusing cross and four side channels that allows for a controlled and fast mixing of the reactants (ESI Fig. S11A, B†). The advantage of microchannels is the presence of a laminar flow without turbulences and therefore a diffusion controlled reaction process for the reactants.[80,81] In a continuous flow, the *s*-SEDMA wCCM dispersion was pumped through the main channel and at the same time, $HAuCl_4 \cdot 3H_2O$ and L-Selectride were fed *via* the side channels (ESI Fig. S11C†). The flow rates were adjusted in a way that allows a direct comparison with the batch *in situ* process as the employed molar ratio of reactants is identical. The flow rate also determines the residence time $t = s\pi R^2/Q$, where s is the length of the capillary (s = 50 mm), R the cross-sectional radius of the capillary (R = 490 μm), and Q the total volumetric flow rate. Here, the total volumetric flow rate is Q = 8000 mL h^{-1}, which corresponds to a residence time of t = 17.0 s. The TEM micrograph reveals that the PDMA patches of the wCCMs are homogeneously and densely loaded with Au NPs, showing an average diameter of D = 4.3 ± 1.4 nm (ESI Fig. S11D†). This is comparable to the size of the Au NPs synthesised by the batch *in situ* reduction (D = 4.7 ± 1.2 nm, Fig. 3A). This indicates that the residence time is sufficiently large to allow for complete reduction of the gold precursor and that the slower mixing in the batch process does not seem to have a major influence on the NP size and homogeneity of the loading. Besides, employing the continuous loading approach the flow rates can be easily varied, which allows a facile tuning of the loading density of the micelles with Au NPs without the need to prepare new reactant solutions (ESI Fig. S11E†).

Binary loading of patchy SEDMA wCCMs

For binary loading of the patchy SEDMA wCCMs with two different types of NPs also the non-functional PS patches need to be loaded. Therefore, we developed a co-precipitation method that offers the possibility to incorporate preformed, PS-stabilised NPs with precisely tailored dimensions within the PS patches of the SEDMA wCCMs without the need for a preceding functionalisation of the patch (Scheme 1B, path C). This method is based on polymer–polymer and polymer–solvent interactions. We chose PS-stabilised Au NPs (PS@Au NPs), which were synthesised by a facile ligand exchange method starting from an aqueous dispersion of citrate-stabilised Au NPs with an average diameter of D = 7.9 ± 0.7 nm (determined by TEM, ESI Fig. S2†) and trithiocarbonate-terminated PS (PS-TTC) in toluene, prepared by RAFT polymerisation (ESI Fig. S3†). After the biphasic ligand exchange, the PS@Au NPs were found to be well dispersed in the organic phase. The TEM micrograph shown in Fig. 4A reveals that the PS@Au NPs are homogeneously distributed on the TEM grid without agglomeration and show a spherical shape. The PS shell is only visible as a pale-grey shell in the TEM micrograph due to the high electron density of the Au NPs.

The PS@Au NPs show a characteristic LSPR at λ_{max} = 527 nm in toluene (Fig. 4B), which is red-shifted by 12 nm with respect to the LSPR of the citrate-stabilised Au NPs in

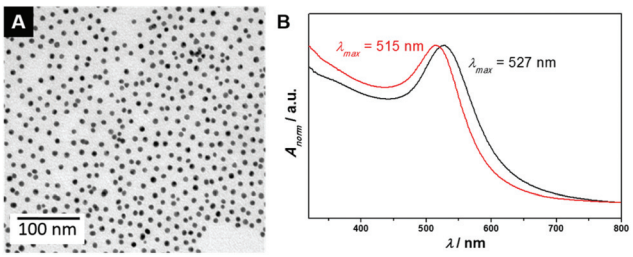

Fig. 4 TEM micrograph (A) and UV-Vis spectrum of PS@Au NPs in toluene (c = 8.8 × 10^{15} NP L^{-1}, black trace in (B)). The red spectrum in (B) corresponds to the citrate-stabilised Au NPs in water (c = 1.2 × 10^{16} NP L^{-1}) recorded prior to the ligand exchange with PS-TTC.

water (λ_{max} = 515 nm). This red-shift is caused by the change in refractive index from the aqueous phase (n = 1.33) to the toluene phase (n = 1.50). DMF-GPC using a UV-Vis diode array detector with two different wavelengths, characteristic for PS (λ = 270 nm) and the Au NPs (λ = 525 nm), shows that the PS-TTC is efficiently bound on the Au NP surface and there is only a small amount of residual free PS ligand (ESI Fig. S4A†). The hydrodynamic radius of the PS@Au NPs was determined by dynamic light scattering to R_h = 14.7 ± 0.1 nm, confirming the PS shell around the Au NPs. First, we investigated the aggregation behaviour of neat PS@Au NPs in THF upon addition of acetone in order to identify suitable conditions for the incorporation of PS@Au NPs in the SEDMA wCCMs *via* co-precipitation. Acetone will be used as the selective solvent for the PDMA patch in the co-precipitation process and, thus, is expected to induce the collapse of the PS ligands. Due to the high sensitivity of the LSPR to particle stability, UV-Vis spectroscopy could be used to follow the solvent induced aggregation (ESI Fig. S12†). Analysis of the spectra reveals that a volume fraction of 33 vol% acetone is sufficient to induce the collapse of the PS shell around the Au NPs, indicated by a broadening of the LSPR, and upon further addition of acetone no significant changes in the UV-Vis absorption maximum were observed.

For co-precipitation, the PS@Au NP dispersion in toluene was mixed with the *s*-SEDMA wCCMs in THF, a good solvent for both the PS and PDMA patches. The details on the used amounts can be found in the Experimental section. The addition of acetone was done in two steps. First, 40 μL acetone (28 vol% with respect to the overall volume) were added in 10 μL portions, employing an equilibration time of 30 min after each addition. Until this point, the PS@Au NPs do not aggregate. However, the solvent quality for PS is slowly decreasing and the PS@Au NPs start to interact with the PS patches of the *s*-SEDMA wCCMs. In the second addition step, the volume fraction of acetone was increased to 90 vol% to ensure a complete co-precipitation of the PS@Au NPs within the PS corona patches. The TEM micrograph of the loaded wCCMs reveals the successful incorporation of the Au NPs within the corona of the *s*-SEDMA wCCMs and shows a clearly visible patch-like arrangement of the Au NPs (Fig. 5A). The PS shell around the

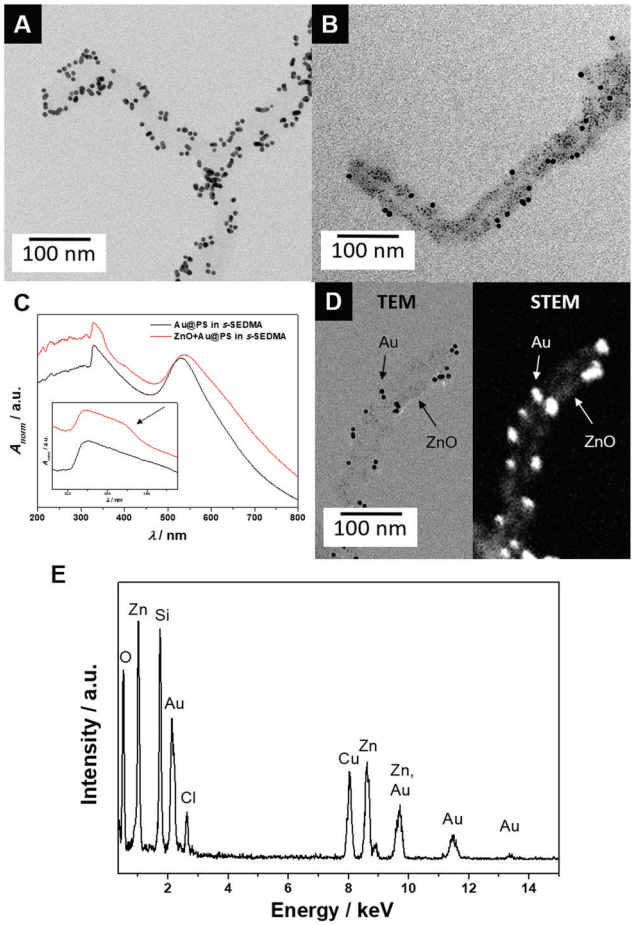

Fig. 5 Hybrid micelles of *s*-SEDMA with PS@Au NPs prepared by co-precipitation (A) and binary loaded *s*-SEDMA wCCMs with PS@Au and ZnO NPs (B). The corresponding UV-Vis spectra are displayed in (C) and the traces were shifted vertically for clarity. Bright-field and HAADF-STEM image (D) and EDX analysis (E) of the binary loaded *s*-SEDMA wCCMs.

Au NPs prevents agglomeration of the NPs even if they are in close proximity to each other. The UV-Vis spectrum clearly shows the LSPR of the Au NPs with a maximum absorbance at λ_{max} = 530 nm (Fig. 5C), which is close to the position of the LSPR of the neat PS@Au NPs (λ_{max} = 527 nm, Fig. 4B). Furthermore, the resonance width did not change significantly and the absorbance quickly drops to values close to zero, which supports the absence of aggregates.

Combining path A and C, binary loading of the patchy wCCMs with ZnO and PS@Au NPs is possible (Scheme 1B). First, the ligand exchange route was employed to incorporate acetate-stabilised ZnO NPs in the PDMA patches of the *s*-SEDMA wCCMs. Subsequently, the PS@Au NPs were loaded into the PS patches by co-precipitation. The overall amount of acetone was adjusted to 90 vol%, as this leads to complete incorporation of the PS@Au NPs. The employed loading sequence is crucial for a successful binary loading of the wCCMs, since the acetate-stabilised ZnO NPs show aggregation in acetone. By exchanging the acetate ligands to PDMA before acetone addition, we prevent the aggregation as shown exemplarily for ZnO loaded *s*-SEDMA wCCMs (ESI Fig. S13†). Consequently, the binary loaded hybrid micelles show no agglomeration of both NP types, but a homogeneous distribution over the whole SEDMA wCCMs, contouring the bright-appearing semi-crystalline polyethylene core (Fig. 5B). We intentionally decreased the amount of incorporated PS@Au NPs in comparison with the sample shown in Fig. 5A to obtain a higher contrast for the ZnO NPs in the TEM micrograph (small dark grey spots within the corona). ICP-OES analysis results in a loading capacity of 56 μg Au and 20 μg ZnO, which corresponds to 43 wt% of inorganic material in the binary loaded wCCMs. These values are similar to the applied amounts of NPs, *i.e.*, 74 μg Au and 28 μg ZnO, respectively.

The UV-Vis spectrum (Fig. 5C) shows the typical LSPR of Au NPs at λ_{max} = 538 nm as well as a signal for the ZnO NPs at λ_{max} = 333 nm, as already observed for the single loaded hybrid micelles (Fig. 2B). The binary loading is further confirmed by high-angle annular dark field scanning transmission electron microscopy (HAADF-STEM, Fig. 5D) and energy dispersive X-ray (EDX) analysis (Fig. 5E). The ZnO NPs in the corona of the binary loaded wCCMs are hardly observable by conventional bright-field TEM (Fig. 5B and D). In HAADF-STEM the contrast is obtained by elastic scattering, only. Thus, the atomic number *Z* of the elements directly affects the contrast of the image. Therefore, the Au NPs appear brighter than the ZnO NPs. Both types of NPs are clearly visible in the HAADF-STEM micrograph (Fig. 5D, marked with arrows) and confirmed by EDX analysis (Fig. 5E) of the same region. As already observed in the bright-field TEM micrograph, the HAADF-STEM image confirms the homogeneous distribution of the Au NPs along the corona of the micelle. The slightly darker appearing ZnO NPs are found in between the Au NPs supporting the patch-like morphology of the corona. The PE core of the SEDMA wCCMs appears as a dark core in between the NP loaded corona, indicating the presence of the polymer template.

The binary loading is not limited to a combination of path A and C. To show the versatility of this method, we combined path B and C to obtain binary loaded wCCMs. To this end, Ag NP loaded hybrid micelles, synthesised by the *in situ* method (same sample like Fig. 3B), were used for subsequent co-precipitation of PS@Au NPs. Due to the significantly different sizes of the NPs (D_{Ag} = 2.9 ± 0.8 nm, D_{Au} = 7.9 ± 0.7 nm), a differentiation of the two NP types in the TEM image is possible (ESI Fig. S14†). Both NP types are well distributed within the wCCM corona and show no agglomeration, underlining the versatility of patchy wCCMs as templates for the preparation of binary loaded hybrid materials.

Conclusions

In this work, we demonstrated that worm-like micelles with a patch-like microphase-separated corona are highly versatile

templates for the regio-selective incorporation of inorganic NPs. Introducing specific anchor groups in one of the corona patches allows to direct the incorporation of metal and metal oxide NPs exclusively in the functionalised patches, either by *in situ* synthesis of the NPs within the patches or by ligand exchange with preformed NPs. In addition, NPs that are stabilised by the same polymer as one of the corona patches can be selectively incorporated by co-precipitation employing selective solvents. The combination of different loading strategies even allows the formation of binary loaded hybrid micelles with two types of NPs placed in different compartments of the patchy wCCM corona. The patchy corona of the worm-like micelles provides an excellent stabilisation of the incorporated NPs. This in turn results in a high and easily accessible catalytically active NP surface area, which is highly favourable for heterogeneous catalysis.[58] The binary loaded hybrid micelles are considered as promising materials for catalytic applications, since the homogeneous distribution of different NPs in the micellar corona ensures a high interface between the NPs. This could enhance synergistic effects on catalysis, as for example reported for the combination of ZnO and Au NPs in the photocatalytic degradation of dyes and antibiotics.[82,83]

Conflicts of interest

There are no conflicts to declare.

Acknowledgements

We thank the German Research Foundation for financial support within the framework of the Collaborative Research Center SFB 840 (project A2). We appreciate support of the Keylab for Optical and Electron Microscopy of the Bavarian Polymer Institute (BPI). The authors thank B. Uch and R. Schneider for GPC and M. Drechsler for help with TEM. J. S. acknowledges the support of the Graduate School of the University of Bayreuth.

References

1 J.-F. Lutz, J.-M. Lehn, E. W. Meijer and K. Matyjaszewski, *Nat. Rev. Mater.*, 2016, **1**, 16024–16037.
2 J. Rodríguez-Hernández, F. Chécot, Y. Gnanou and S. Lecommandoux, *Prog. Polym. Sci.*, 2005, **30**, 691–724.
3 J.-F. Gohy, in *Block Copolymers II*, Springer-Verlag, Berlin/Heidelberg, 2005, vol. 190, pp. 65–136.
4 Y. Mai and A. Eisenberg, *Chem. Soc. Rev.*, 2012, **41**, 5969–5985.
5 J. Dupont, G. Liu, K. I. Niihara, R. Kimoto and H. Jinnai, *Angew. Chem., Int. Ed.*, 2009, **48**, 6144–6147.
6 S. Zhong, H. Cui, Z. Chen, K. L. Wooley and D. J. Pochan, *Soft Matter*, 2008, **4**, 90–93.
7 I. S. Jo, S. Lee, J. Zhu, T. S. Shim and G. R. Yi, *Curr. Opin. Colloid Interface Sci.*, 2017, **30**, 97–105.
8 A. O. Moughton, M. A. Hillmyer and T. P. Lodge, *Macromolecules*, 2012, **45**, 2–19.
9 J. Du and R. K. O'Reilly, *Chem. Soc. Rev.*, 2011, **40**, 2402–2416.
10 A. Walther and A. H. E. Müller, *Chem. Rev.*, 2013, **113**, 5194–5261.
11 D. J. Pochan, J. Zhu, K. Zhang, K. L. Wooley, C. Miesch and T. Emrick, *Soft Matter*, 2011, **7**, 2500–2506.
12 D. J. Pochan, *Science*, 2004, **306**, 94–97.
13 H. Cui, Z. Chen, S. Zhong, K. L. Wooley and D. J. Pochan, *Science*, 2007, **317**, 647–650.
14 A. H. Gröschel and A. H. E. Müller, *Nanoscale*, 2015, **7**, 11841–11876.
15 U. Tritschler, S. Pearce, J. Gwyther, G. R. Whittell and I. Manners, *Macromolecules*, 2017, **50**, 3439–3463.
16 Z. Li, M. A. Hillmyer and T. P. Lodge, *Langmuir*, 2006, **22**, 9409–9417.
17 A. H. Gröschel, A. Walther, T. I. Löbling, F. H. Schacher, H. Schmalz and A. H. E. Müller, *Nature*, 2013, **503**, 247–251.
18 T. I. Löbling, O. Borisov, J. S. Haataja, O. Ikkala, A. H. Gröschel and A. H. E. Müller, *Nat. Commun.*, 2016, **7**, 12097–12106.
19 J. Hu, G. Liu and G. Nijkang, *J. Am. Chem. Soc.*, 2008, **130**, 3236–3237.
20 F. H. Schacher, P. A. Rupar and I. Manners, *Angew. Chem., Int. Ed.*, 2012, **51**, 7898–7921.
21 R. K. O'Reilly, C. J. Hawker and K. L. Wooley, *Chem. Soc. Rev.*, 2006, **35**, 1068–1083.
22 T. H. Epps III and R. K. O'Reilly, *Chem. Sci.*, 2016, **7**, 1674–1689.
23 J. Schmelz, F. H. Schacher and H. Schmalz, *Soft Matter*, 2013, **9**, 2101–2107.
24 X. Wang, G. Guerin, H. Wang, Y. Wang, I. Manners and M. A. Winnik, *Science*, 2007, **317**, 644–647.
25 J. B. Gilroy, T. Gädt, G. R. Whittell, L. Chabanne, J. M. Mitchels, R. M. Richardson, M. A. Winnik and I. Manners, *Nat. Chem.*, 2010, **2**, 566–570.
26 T. Gädt, N. S. Ieong, G. Cambridge, M. A. Winnik and I. Manners, *Nat. Mater.*, 2009, **8**, 144–150.
27 F. He, T. Gädt, I. Manners and M. A. Winnik, *J. Am. Chem. Soc.*, 2011, **133**, 9095–9103.
28 P. A. Rupar, L. Chabanne, M. A. Winnik and I. Manners, *Science*, 2012, **337**, 559–562.
29 J. Qian, Y. Lu, A. Chia, M. Zhang, P. A. Rupar, N. Gunari, G. C. Walker, G. Cambridge, F. He, G. Guerin, I. Manners and M. A. Winnik, *ACS Nano*, 2013, **7**, 3754–3766.
30 J. R. Finnegan, D. J. Lunn, O. E. C. Gould, Z. M. Hudson, G. R. Whittell, M. A. Winnik and I. Manners, *J. Am. Chem. Soc.*, 2014, **136**, 13835–13844.
31 Z. M. Hudson, D. J. Lunn, M. A. Winnik and I. Manners, *Nat. Commun.*, 2014, **5**, 3372–3379.
32 Z. M. Hudson, C. E. Boott, M. E. Robinson, P. A. Rupar, M. A. Winnik and I. Manners, *Nat. Chem.*, 2014, **6**, 893–898.

33 H. Qiu, Y. Gao, V. A. Du, R. Harniman, M. A. Winnik and I. Manners, *J. Am. Chem. Soc.*, 2015, **137**, 2375–2385.
34 H. Qiu, Z. M. Hudson, M. A. Winnik and I. Manners, *Science*, 2015, **347**, 1329–1332.
35 X. Li, Y. Gao, C. E. Boott, M. A. Winnik and I. Manners, *Nat. Commun.*, 2015, **6**, 8127–8134.
36 X. Li, Y. Gao, C. E. Boott, D. W. Hayward, R. Harniman, G. R. Whittell, R. M. Richardson, M. A. Winnik and I. Manners, *J. Am. Chem. Soc.*, 2016, **138**, 4087–4095.
37 H. Schmalz, J. Schmelz, M. Drechsler, J. Yuan, A. Walther, K. Schweimer and A. M. Mihut, *Macromolecules*, 2008, **41**, 3235–3242.
38 B. Fan, L. Liu, J.-H. Li, X.-X. Ke, J.-T. Xu, B.-Y. Du and Z.-Q. Fan, *Soft Matter*, 2016, **12**, 67–76.
39 L. Sun, A. Pitto-Barry, A. W. Thomas, M. Inam, K. Doncom, A. P. Dove and R. K. O'Reilly, *Polym. Chem.*, 2016, **7**, 2337–2341.
40 L. Sun, A. Pitto-Barry, N. Kirby, T. L. Schiller, A. M. Sanchez, M. A. Dyson, J. Sloan, N. R. Wilson, R. K. O'Reilly and A. P. Dove, *Nat. Commun.*, 2014, **5**, 5746–5754.
41 J. Qian, X. Li, D. J. Lunn, J. Gwyther, Z. M. Hudson, E. Kynaston, P. A. Rupar, M. A. Winnik and I. Manners, *J. Am. Chem. Soc.*, 2014, **136**, 4121–4124.
42 J. Li, X. Li, D. Ni, J. Wang, G. Tu and J. Zhu, *J. Appl. Polym. Sci.*, 2014, **131**, 41186–41196.
43 G. Rizis, T. G. M. van de Ven and A. Eisenberg, *Soft Matter*, 2014, **10**, 2825–2835.
44 J. Wang, W. Zhu, B. Peng and Y. Chen, *Polymer*, 2013, **54**, 6760–6767.
45 J. Schmelz, M. Karg, T. Hellweg and H. Schmalz, *ACS Nano*, 2011, **5**, 9523–9534.
46 S. Rosenfeldt, F. Lüdel, C. Schulreich, T. Hellweg, A. Radulescu, J. Schmelz, H. Schmalz and L. Harnau, *Phys. Chem. Chem. Phys.*, 2012, **14**, 12750–12756.
47 J. Schmelz, A. E. Schedl, C. Steinlein, I. Manners and H. Schmalz, *J. Am. Chem. Soc.*, 2012, **134**, 14217–14225.
48 Y. Mai and A. Eisenberg, *Acc. Chem. Res.*, 2012, **45**, 1657–1666.
49 S. Suárez-Suárez, G. A. Carriedo and A. P. Soto, *Chem. – Eur. J.*, 2015, **21**, 14129–14139.
50 B. Nandan and A. Horechyy, *ACS Appl. Mater. Interfaces*, 2015, **7**, 12539–12558.
51 M. Changez, N.-G. Kang, D. W. Kim and J.-S. Lee, *Nanoscale*, 2013, **5**, 11554–11560.
52 K. H. Ku, J. M. Shin, M. P. Kim, C. H. Lee, M. K. Seo, G. R. Yi, S. G. Jang and B. J. Kim, *J. Am. Chem. Soc.*, 2014, **136**, 9982–9989.
53 F. Schacher, E. Betthausen, A. Walther, H. Schmalz, D. V. Pergushov and A. H. E. Müller, *ACS Nano*, 2009, **3**, 2095–2102.
54 R. J. Hickey, Q. Luo and S. J. Park, *ACS Macro Lett.*, 2013, **2**, 805–808.
55 M. P. Kim, K. H. Ku, H. J. Kim, S. G. Jang, G. R. Yi and B. J. Kim, *Chem. Mater.*, 2013, **25**, 4416–4422.
56 A. Walther, J. Yuan, V. Abetz and A. H. E. Müller, *Nano Lett.*, 2009, **9**, 2026–2030.
57 Y. Guo, S. Harirchian-Saei, C. M. S. Izumi and M. G. Moffitt, *ACS Nano*, 2011, **5**, 3309–3318.
58 J. Schöbel, M. Burgard, C. Hils, R. Dersch, M. Dulle, K. Volk, M. Karg, A. Greiner and H. Schmalz, *Angew. Chem., Int. Ed.*, 2017, **56**, 405–408.
59 H. Wang, W. Lin, K. P. Fritz, G. D. Scholes, M. A. Winnik and I. Manners, *J. Am. Chem. Soc.*, 2007, **129**, 12924–12925.
60 H. Wang, X. Wang, M. A. Winnik and I. Manners, *J. Am. Chem. Soc.*, 2008, **130**, 12921–12930.
61 H. Wang, A. J. Patil, K. Liu, S. Petrov, S. Mann, M. A. Winnik and I. Manners, *Adv. Mater.*, 2009, **21**, 1805–1808.
62 F. H. Schacher, T. Rudolph, M. Drechsler and A. H. E. Müller, *Nanoscale*, 2011, **3**, 288–297.
63 S. G. Jang, D. J. Audus, D. Klinger, D. V. Krogstad, B. J. Kim, A. Cameron, S. W. Kim, K. T. Delaney, S. M. Hur, K. L. Killops, G. H. Fredrickson, E. J. Kramer and C. J. Hawker, *J. Am. Chem. Soc.*, 2013, **135**, 6649–6657.
64 L. Jia, G. Zhao, W. Shi, N. Coombs, I. Gourevich, G. C. Walker, G. Guerin, I. Manners and M. A. Winnik, *Nat. Commun.*, 2014, **5**, 3882–3889.
65 J. Xu, H. Zhou, Q. Yu, I. Manners and M. Winnik, *J. Am. Chem. Soc.*, 2018, **140**, 2619–2628.
66 S. H. Jo, H. W. Kim, M. Song, N. J. Je, S. H. Oh, B. Y. Chang, J. Yoon, J. H. Kim, B. Chung and S. Yoo II, *ACS Appl. Mater. Interfaces*, 2015, **7**, 18778–18785.
67 S. Mei, J. Cao and Y. Lu, *J. Mater. Chem. A*, 2015, **3**, 3382–3389.
68 J. Schöbel, M. Karg, D. Rosenbach, G. Krauss, A. Greiner and H. Schmalz, *Macromolecules*, 2016, **49**, 2761–2771.
69 C. Bojer, J. Schöbel, T. Martin, M. Ertl, H. Schmalz and J. Breu, *Appl. Catal., B*, 2017, **204**, 561–565.
70 T. Kida, T. Oka, M. Nagano, Y. Ishiwata and X. G. Zheng, *J. Am. Ceram. Soc.*, 2007, **90**, 107–110.
71 J. Piella, N. G. Bastús and V. Puntes, *Chem. Mater.*, 2016, **28**, 1066–1075.
72 G. Moad, J. Chiefari, Y. K. Chong, J. Krstina, R. T. A. Mayadunne, A. Postma, E. Rizzardo and S. H. Thang, *Polym. Int.*, 2000, **49**, 993–1001.
73 A. C. Henry, T. J. Tutt, M. Galloway, Y. Y. Davidson, C. S. McWhorter, S. A. Soper and R. L. McCarley, *Anal. Chem.*, 2000, **72**, 5331–5337.
74 S. Ehlert, S. M. Taheri, D. Pirner, M. Drechsler, H. W. Schmidt and S. Förster, *ACS Nano*, 2014, **8**, 6114–6122.
75 M. R. Jones, K. D. Osberg, R. J. MacFarlane, M. R. Langille and C. A. Mirkin, *Chem. Rev.*, 2011, **111**, 3736–3827.
76 S. W. B. Schonecker, *Makromol. Chem.*, 1996, **338**, 759–762.

77 T. Hendel, M. Wuithschick, F. Kettemann, A. Birnbaum, K. Rademann and J. Polte, *Anal. Chem.*, 2014, **86**, 11115–11124.
78 N. R. Jana, L. Gearheart and C. J. Murphy, *Langmuir*, 2001, **17**, 6782–6786.
79 H. Pletsch, L. Peng, F. Mitschang, A. Schaper, M. Hellwig, D. Nette, A. Seubert, A. Greiner and S. Agarwal, *Small*, 2014, **10**, 201–208.
80 G. M. Whitesides, *Nature*, 2006, **442**, 368–373.
81 R. Karnik, F. Gu, P. Basto, C. Cannizaro, L. Dean, W. Kyei-Manu, R. Langer and O. C. Farokhzad, *Nano Lett.*, 2008, **8**, 2906–2912.
82 C. Bojer, J. Schöbel, T. Martin, T. Lunkenbein, D. R. Wagner, A. Greiner, J. Breu and H. Schmalz, *Polymer*, 2017, **128**, 65–70.
83 L. Sun, D. Zhao, Z. Song, C. Shan, Z. Zhang, B. Li and D. Shen, *J. Colloid Interface Sci.*, 2011, **363**, 175–181.